



Mechanochemical enhancement in electrode materials via silver-embedded reduced graphene oxide and cobalt oxide nanostructure for supercapacitor applications

Aliaa Abdelfattah¹ · Fatma M. Ahmed^{2,3} · Lamiaa Z. Mohamed¹ · Ahmed M. Selim^{1,2}

Received: 12 November 2023 / Revised: 19 December 2023 / Accepted: 9 January 2024 / Published online: 23 January 2024
© The Author(s) 2024

Abstract

This study delves into the intricate domain of mechanochemical synthesis, employing a developed approach for the fabrication of electrode materials. The method involves the incorporation of silver nanoparticles into a two-dimensional matrix of reduced graphene oxide (RGO) combined with cobalt oxide nanostructures, yielding a zero-dimensional cobalt oxide@RGO.Ag nanocomposite. A comprehensive suite of material characterization techniques, including XRD, SEM, EDX, TEM, XPS, and BET, was used to investigate the synthesized materials. Concurrently, extensive electrochemical investigations, incorporating cyclic voltammetry (CV), galvanic charge–discharge (GCD), electrochemical impedance spectroscopy (EIS), and retention analyses, are applied to the constructed electrochemical cell. The resulting RGO.Ag@Co₃O₄ nanocomposite exhibits a remarkable specific capacitance of 371.2 F g⁻¹ at a scan rate of 5 mV s⁻¹. In addition, energy density (Ed) and power density (Pd) values of 21.6 Wh/kg and 997 W/kg, respectively, are achieved at a current density (Cd) of 0.5 A g⁻¹.

Keywords Reduced graphene oxide · Silver · Cobalt oxide · Nanostructure · Supercapacitor

Introduction

In response to the increasing reliance on electronic devices, the demand for efficient and environmentally friendly energy storage systems has grown significantly. Supercapacitors (SCs), often known as ultracapacitors or electrochemical capacitors, are a sort of energy storage device that has garnered a significant amount of consideration in recent years since they have a high-power density (P_d), rapid charge/discharge rate, a long cycle life, and excellent stability [1, 2]. Typically composed of two electrodes, an electrolyte, and a separator, standard SCs rely significantly on the performance of their electrodes, which serves as the primary determinant

of overall device efficacy. While SCs possess lower energy densities (E_{ds}) compared to batteries, constraining their utility in power supply applications, significant research has been dedicated to exploring the utilization of nanostructured electrode materials. This attempt aims to enhance both the energy densities (E_{ds}) and power densities (P_{ds}) of SCs, thereby expanding their potential for diverse applications [3, 4].

According to the unique attributes of graphene, such as its substantial surface area, excellent electrical conductivity, and mechanical durability, it has emerged as a promising candidate for electric double-layer capacitor (EDLC) electrodes utilized in energy storage applications. However, graphene-based electrodes suffer from the drawback of having a low specific capacitance, limiting their applicability in various fields [5–8]. To overcome this limitation, potential solutions such as doping with heteroatoms, chemical functionalization, and hybridization with other materials have been proposed [9–12]. Conversely, silver is a viable choice for supercapacitor (SC) electrodes due to its affordability and widespread availability. Interestingly, incorporating silver nanoparticles into graphene layers has the potential to efficiently promote charge transfer and increase specific capacitance, ultimately boosting the

✉ Lamiaa Z. Mohamed
Lamiaa.zaky@Cu.edu.eg

¹ Mining, Petroleum, and Metallurgical Engineering Department, Faculty of Engineering, Cairo University, Giza 12613, Egypt

² Nanotechnology Lab, Electronics Research Institute, Cairo 12622, Egypt

³ Physics Department, Faculty of Science, Cairo University, Giza 12613, Egypt

energy and power density of the SCs. Additionally, silver nanoparticles can serve as catalysts, promoting faster redox reactions at the electrode–electrolyte interface. Furthermore, adding silver nanoparticles to graphene can mitigate graphene's tendency to restack, promoting improved electrode electrocatalytic activity and resulting in faster charge and discharge rates. Consequently, the composite material, decorated with silver nanoparticles on graphene, emerges as a compelling choice for developing high-performance supercapacitors with superior electrochemical attributes [13].

In contrast, pseudocapacitors (PCs), which depend on quick faradic charge transfer mechanisms, extensively use electrode nanomaterials mostly derived from conducting polymers and/or transition metal oxides. Consequently, PCs can attain higher specific capacitance and superior energy density (E_d) compared to electric double-layer capacitors (EDLCs) [5]. Furthermore, extensive studies have focused on blending carbon nanostructures and nanomaterials to create hybrid nanocomposite electrodes for supercapacitors (SCs). This approach addresses balancing energy and power in developing advanced SCs. This method is anticipated to yield significant improvements in specific capacitance, energy density (E_d), and high-power density (P_d) [14, 15]. In addition, cobalt oxide nanostructures have emerged as key components in SCs, offering a range of functionalities that enhance their electrochemical performance. Due to their effect on exceptional ionic conductivity, cobalt oxide nanostructures provide an ideal platform for efficient charge storage. The Faradaic charge transfer mechanisms substantially increase specific capacitance, resulting in superior energy density and prolonged cycle life. Furthermore, their inherent stability ensures the long-term reliability of SCs, making them well-suited for various applications. The versatile nature of cobalt oxide nanostructures positions them as a vital catalyst in the evolution of high-performance SCs [16, 17].

Besides, the two-electrode configuration SCs are pivotal in assessing and optimizing their performance. This setup is crucial for accurately measuring the specific capacitance, energy density, and power density of SC materials and designs. Utilizing this setup allows for the effective storage and discharge of electric energy, rendering SCs indispensable components across various applications, from portable electronics to renewable energy systems. Moreover, the two-electrode arrangement streamlines the assessment of cycle longevity, charge–discharge effectiveness, and broader electrochemical performance, providing valuable perspectives on the suitability and trustworthiness of SCs for particular purposes. This configuration is essential for scientists and engineers striving to enhance energy storage technologies and address the escalating need for efficient and eco-friendly power solutions [18].

The benefits of hybrid electrodes, two types of electrodes merged into one device, have been the subject of several studies (SCs). To be more precise, Xiaomin et al. created 3D hierarchical porous carbon scaffold-MnO₂ (3D-HPCS@MnO₂) nanohybrids with colony-similar microstructures that directed to a gravimetric specific capacitance of 231.5 F g⁻¹ and excellent cycling performance (95% capacitance retention after 10,000 cycles). It was an asymmetric SC-based on HPCS/HPCS@MnO₂ with a P_d associated with 20.7 kW kg⁻¹ and E_d of 60.8 Wh kg⁻¹ [16]. Mahmut et al. created binder-free PANI@MnO₂@PCNF SC-electrodes by electrodepositing MnO₂ nanoparticles onto electrospun PCNFs and then chemically polymerizing aniline on the MnO₂@PCNF composite. These electrodes exhibited extreme capacitance retention (91%) after 1000 cycles with a capacitance of 289 F g⁻¹ [19]. In addition, Jun Hu et al. [20] devised a straightforward hydrothermal technique for producing NiO-loaded nitrogen-doped reduced graphene oxide (NiO/N-rGO) composites. These composites showed excellent electrochemical performance, with specific capacitances reaching up to 233 F g⁻¹ at 1 A g⁻¹ when the solution was composed of 6M KOH. S. Kong et al. [21] created a composite electrode by combining nanostructured MnO₂ with porous activated carbon (PAC). This combination resulted in a high specific capacitance of 258 F g⁻¹ at 1 A g⁻¹ and improved rate performance with 82.8% capacitance retention across a current density (C_d) range of 1 A g⁻¹ till 20 A g⁻¹.

In this research, we introduced a novel approach for the mechanochemical synthesis of advanced electrode materials with distinctive characteristics. A key innovation lies in the utilization of a straightforward and highly efficient technique to fabricate an exclusive unique two-dimensional reduced graphene oxide (2D RGO) adorned with a conductive silver nanostructure. This hybrid material was further enhanced by the incorporation of zero-dimensional (0D) cobalt oxide nanostructures through a precise high-energy ball milling process. This resulted in an exceptional nanocomposite electrode material with promising supercapacitor (SC) applications. Subsequently, the composite material was thoroughly characterized and subjected to electrochemical testing to evaluate the performance within SCs using a 6 M KOH alkaline electrolyte.

Experimental section

Preparation of graphene oxide

The used chemical substances and supplies were acquired from Alpha Aesar and had a grade level of at least 99.5% without requiring any further processing on the part of the purchaser. Producing graphene oxide was accomplished by a controlled version of the Hummer method in this recently

published research. In conclusion, a magnetic stirrer combined 5 g of fine graphite powder with 120 mL of H₂SO₄ while stirring the mixture for 30 min. The next step was the addition of 2.5 g of powdered sodium nitrate. Then, putting the solution in an ice bath, 15 g of potassium permanganate (KMnO₄) particles was added. This was done gradually over 1 h until a solution with a deep green color was achieved. The temperature was increased to 35 °C while the mixture was stirred for 30 min. After heating the mix, a slow and steady stream added 230 ml of distilled water. After that, the temperature (T) was allowed to boil for half an hour while continuously stirring. As soon as the solution had reached a dark brown color, 500 ml of DW and 50 ml of H₂O₂ with a concentration of 30% were added gradually. Upon washing the liquid with DW and ethanol, 50 ml of 0.1 M HCl was put in to remove metal deposits. This was done to ensure no metal traces remained (50:50). Following filtering and many washes in DW, the resulting GO powder was a dark brown. This powder was dried at 60 °C in a vacuum oven for 12 h.

Preparation of nanosilver-entrapped RGO

After dispersing 1 g of GO powder across 300 ml of DW using an ultrasonic bath, the mixture was sonicated for 2 h. After that, 176.39 mg of AgNO₃ was put into the solution, first dissolved in 10 ml of DW before being heated for half an hour. To reduce GO and AgNO₃, hydrazine hydrate was added to the mixture, which was then heated to 100 °C in a hot water bath for 3 h while being agitated. The recovered powder was dried in a vacuum for 12 h furnace at 60 °C after being washed and cleaned with DW and ethanol.

Preparation of 0D cobalt oxide@RGO-Ag nanocomposite

Mechanical milling employing high-energy balls was employed as a one-step procedure for the production of nanocomposites. Concisely, 133.33 mg of 99.9% pure cobalt oxide, characterized by an average particle size of 5 microns, was introduced to the previously synthesized RGO-Ag. Subsequently, the composite was transferred to high-energy ball milling using a FRETCH “GERMANY, High Energy Ball Mill, Type E max” system for 3 h. The milling process operated at a rotational speed of 1500 revolutions per minute, utilizing 10-mm-diameter 304 stainless steel balls with a ball-to-weight ratio of (9:1). Following milling, the resulting nanocomposite was subjected to a cleaning process involving a mixture of ethanol and deionized water (50:50). The schematic diagram for synthesis process is illustrated in Fig. 1.

Electrode fabrication

The standard process for generating cell electrodes was as follows: a weight ratio of 92% as-synthesized active material to 8% PVDF (polyvinylidene fluoride) created by immersion in organic binder NMP (N-methyl-2-pyrrolidone). This mixture was then automatically deposited over a graphite foil (0.1 mm thick) as a current collector. Then, the film was divided into two identical carbon electrodes with 0.9 cm in diameter and a total active material of 4 mg using an MSK-T-06 precision disc cutter. The electrodes were then vacuum-dried at 60 °C with 4 mg/cm² active material. In a

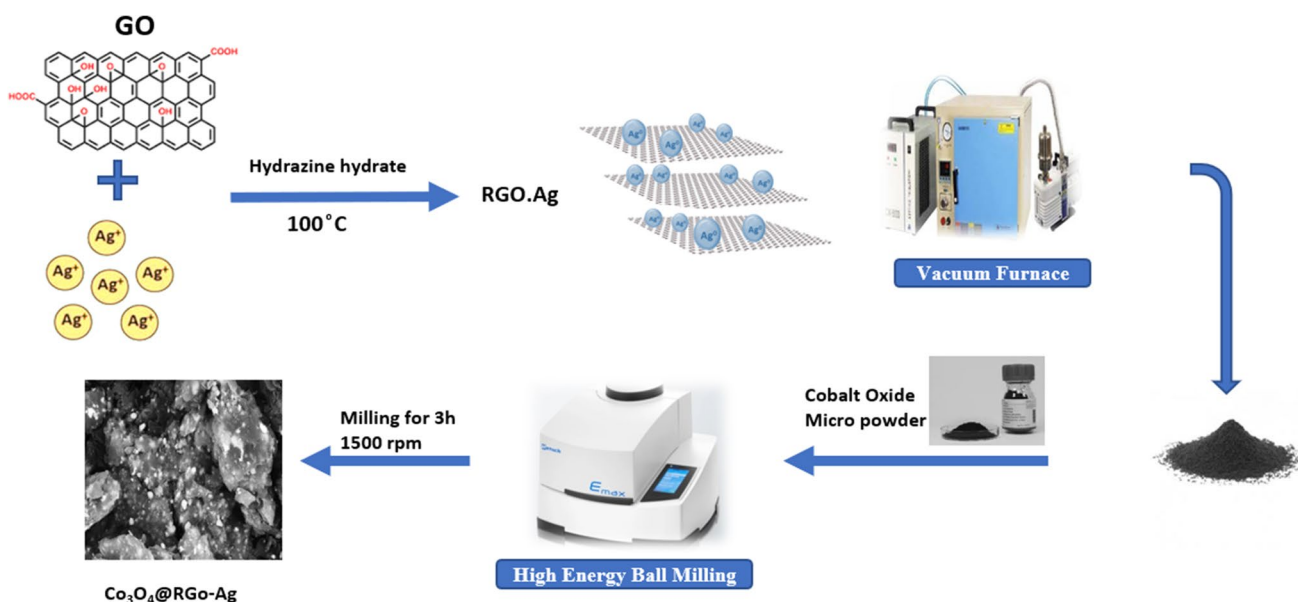


Fig. 1 Schematic diagram for the synthesis process of nanostructure RGO-Ag@Co₃O₄

Swagelok test cell for a whole package SC, 6 M KOH solution was used as the alkaline electrolyte, and glass fibers were used as the separator.

Material characterizations

Phase identification

The X-ray diffraction (XRD) model was used to investigate the nanomaterials' phases and lattice structure after manufacturing using the Smartlab Hypix 3000 system— λ Cu K α = 0.154 nm—RigaKo, Japan.

Morphology and composition

Scanning electron microscopy (SEM), model NRC QUANTA FEG-250, and an energy dispersive X-ray analysis (EDX) detector, model Octan pro-Det, were utilized to investigate surface morphology and chemical analysis. High-resolution transmission electron microscopy (TEM), model JEM 2100 HRTEM, made in Japan, was used to examine the distribution of nanostructure elements.

X-ray photoelectron spectroscopy

X-ray photoelectron spectroscopy (XPS) employed model X-ray Al K α radiation at energies ranging from 10 to

1350 eV, and a spot size of 400 μ m at 200 eV was carried out to conduct additional composite evaluation.

Electrochemical characterizations

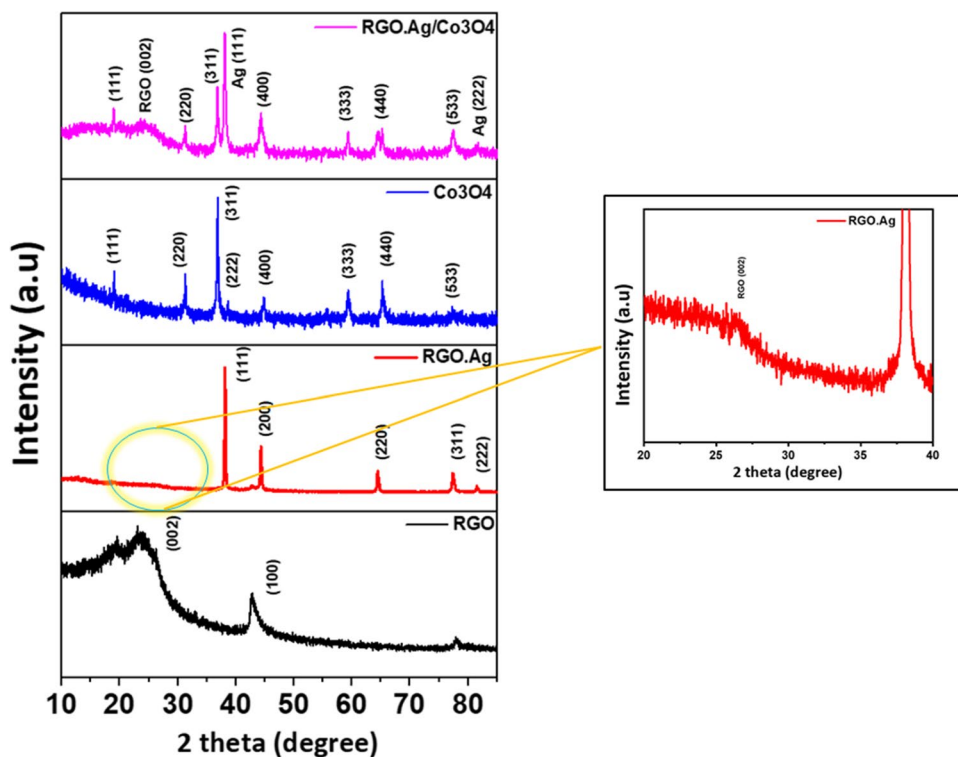
Electrochemical characterizations use the Potentiostat VSP 300 (Fig. 1b) at room temperature with two electrodes. The cyclic voltammetry (CV) experiment was carried out by scanning through a potential window of 0 to 1 V at various scan speeds (ranging from 5 to 5 to 100 mV s^{-1}). During the same period, galvanostatic charge–discharge (GCD) plots were assessed using a variety of current densities. Additionally, electrochemical impedance spectroscopy (EIS) with a Nyquist plot was carried out across the 0.1 Hz to 100 kHz frequency range, and the retention test of the constructed SC was evaluated at C_d of 2 Ag^{-1} to complete the research.

Results and discussions

Phase identification

Figure 2 describes the XRD patterns of RGO (reduced graphene oxide), RGO decorated with silver (RGO-Ag), and RGO-Ag integrated with cobalt oxide (RGO-Ag@Co₃O₄). The RGO spectrum, as illustrated in Fig. 2, reveals two prominent peaks, with 2θ values of 25.33° and 42.59°, related to (002) and (100) planes, respectively. The former

Fig. 2 The XRD results of as-synthesized **a** RGO, **b** RGO-Ag, **c** Co₃O₄, and **d** RGO-Ag@Co₃O₄



peak exhibits broadness due to interlayer spacing, indicating the amorphous nature of the RGO [22]. The RGO board peak at 23° corresponds to the (002) crystalline plane [23–25]. A slight shift of the primary peak (25.33°) from 23° in RGO may be attributed to the high degree of reduction [26], which leads to the oxygen functional groups decomposition and the fewer sp^2 -hybridized carbon domains creation [27, 28]. The RGO-Ag pattern displays the reduced intensity of RGO peaks, indicating the formation of a new crystalline material with high crystallinity. This new material exhibits sharp peaks with a face-centered cubic (FCC) structure at 38.02° , 44.13° , 64.43° , 77.36° , and 81.69° , connected to the (111), (200), (220), (311), and (222) planes, respectively [29–31]. The functionalized RGO-Ag@ Co_3O_4 pattern shows peaks at 19° , 25.33° , 31° , 37° , 38.02° , 44.13° , 59.4° , 64.43° , 77.36° , and 81.69° , indicating the presence of RGO (25.33°) and RGO-Ag (38.02° , 44.13° , 64.43° , 77.36° , and 81.69°). The emergence of new peaks at 18.99° , 31.2° , 36.8° , 59.4° , and 65.3° signifies the formation of Co_3O_4 nanostructure [32–34].

Morphology and composition

Figures 3, 4, and 5 depict the morphological characteristics and elemental composition of the prepared powders. Accordingly, Fig. 3 and Fig. S1 present SEM images at various magnifications, offering insights into the as-synthesized materials and their respective compositions. The distribution of silver nanoparticles between the RGO layers is visually demonstrated in Fig. 3b, highlighting a homogeneous arrangement. Besides, the morphology of the Co_3O_4 exhibits equiaxed grains, as evidenced by Fig. 3c. Furthermore, the composite RGO-Ag@ Co_3O_4 demonstrates uniform distribution, as depicted in Fig. 2d, indicating a homogeneous disposition of Co_3O_4 powders within the composite. This even distribution of silver and the composite structure contributes to a high surface area and favorable charge storage, as supported by previous findings [35]. In addition, Fig.S2 presents the EDX patterns and chemical compositions of RGO, RGO-Ag, Co_3O_4 , and RGO-Ag@ Co_3O_4 . The EDX results confirm the successful preparation of RGO-Ag and RGO-Ag@ Co_3O_4 powders, illustrating their coexistence with RGO, Ag, and Co_3O_4 components.

Fig. 3 The SEM micrographs of **a** RGO, **b** RGO-Ag, **c** cobalt oxide, and **d** RGO-Ag@ Co_3O_4

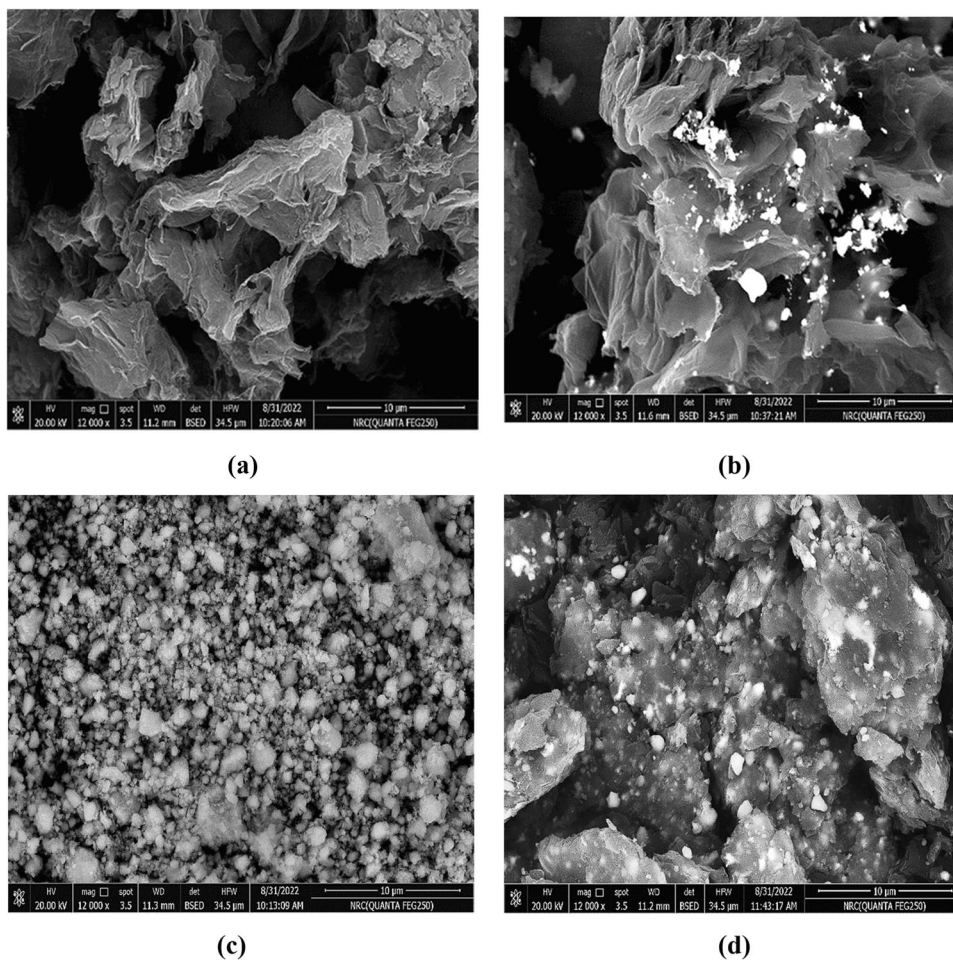


Fig. 4 The TEM images of **a** 2D RGO, **b** RGO-Ag, **c** Co_3O_4 nanoparticles, and **d** RGO-Ag@ Co_3O_4

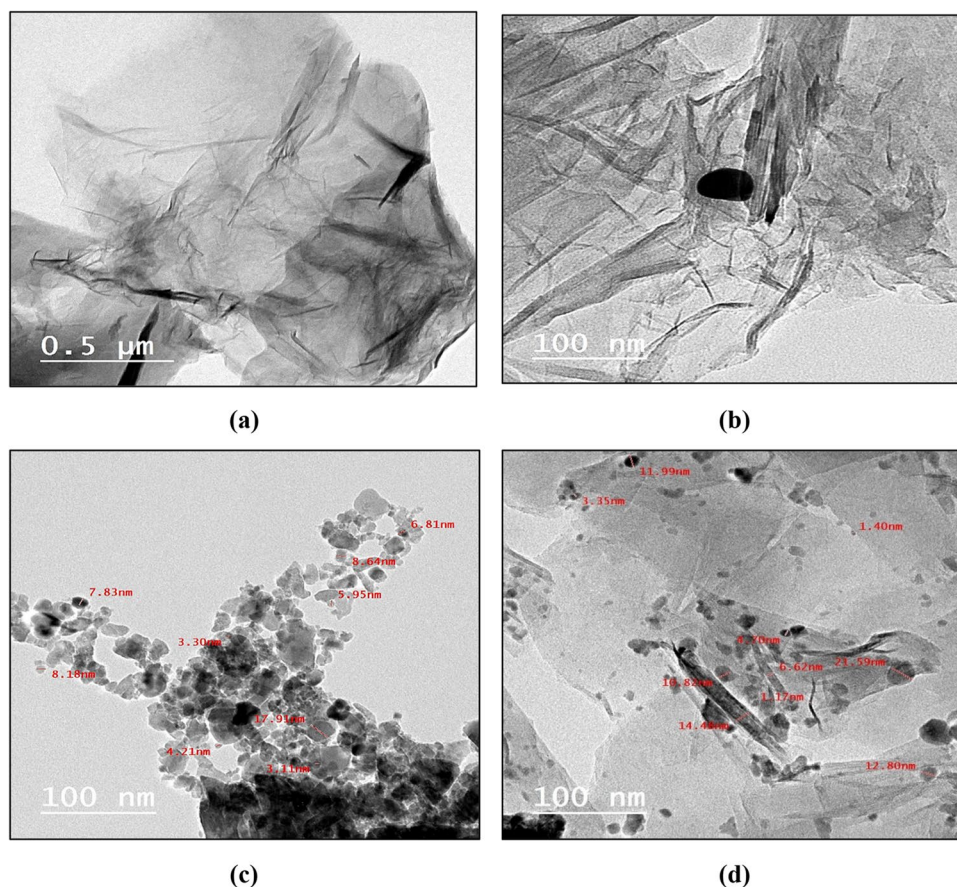


Fig. 5 **a** The isotherms and **b** the BJH of RGO, RGO-Ag, and RGO-Ag/RGO

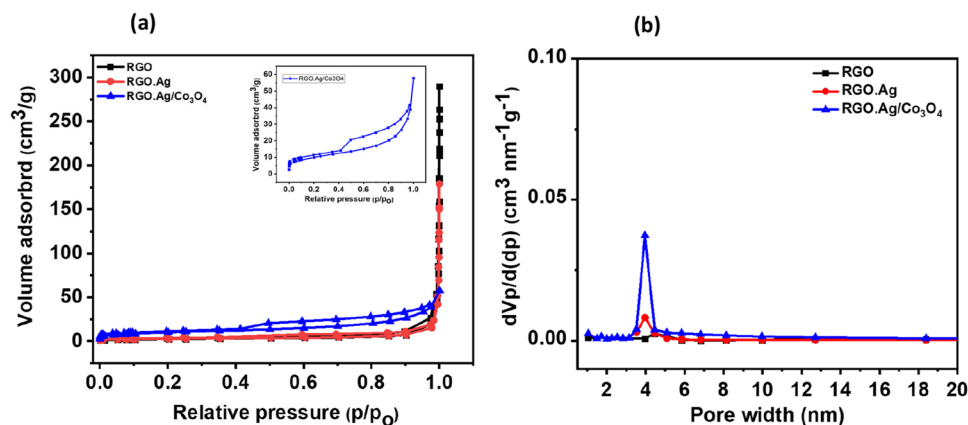


Figure 4 and Fig. S3 demonstrate the TEM micrographs at different magnifications offering a detailed view of the as-prepared powders. The particle size obtained from cobalt oxide exhibits an average size of 7.32 nm. The TEM morphology serves to enhance our understanding of the characteristics of the prepared active materials. The effective distribution of Ag within the composite promotes the restriction of restacking the nature of RGO sheets together [35]. The incorporation of Ag into RGO nanosheets elucidates a strong interaction, ultimately enhancing the

electrical performance of the prepared RGO [36]. Furthermore, the addition of Ag nanoparticles or composite materials introduces a notable observation that certain particles tend to agglomerate within the overall structure [37, 38].

BET illustrates crucial details about the material's surface area, mean pore diameter, and volume. The samples undergo a 6-h degassing process at 130 °C. According to the International Union of Pure and Applied Chemistry (IUPAC), Fig. 5a depicts the adsorption–desorption isotherms, which showed the isotherm was between types I and IV [39].

IUPAC describes the adsorption hysteresis in the inset of Fig. 5a as an H3 type.

The specific surface areas (S_{BET}) of the prepared samples are reported in Table 1. According to the data in this table, the surface area of RGO was 8.4 m²/g and increased to 9 m²/g after adding Ag this small S_{BET} could be due to the thermal treatment and restacking of the sheet during preparation [40]. Furthermore, the RGO.Ag/Co₃O₄ composite had the highest surface area of 35 m²/g, indicating doping via cobalt oxide in the cavity between the RGO.Ag nanosheets prevented restacking and increased the surface area [41, 42]. The Barrett Joyner Halenda (BJH) model was used to estimate the pore size distribution of the composites. The results are shown in Fig. 5b and Table 1, which confirm an excellent mesoporous structure. The composite had a variety of pore types, which aided charge transfer and ensured active site exposure.

X-ray photoelectron spectroscopic analysis

X-ray photoelectron spectroscopy (XPS) was applied to explore the composite’s chemical composition and bonding states. The prepared sample survey spectrums are described in Fig. 6, which revealed the existence of several elements, such as carbon (C), oxygen (O), nitrogen (N), cobalt (Co), and silver (Ag), with corresponding binding energies of 285.34, 532.53, 401.06, 781.28, and 369.02 eV, respectively. The C 1s spectrum, Fig. 7b, exhibited four distinct peaks at 284.48 eV, 285.58 eV, 286.38 eV, and 287.68 eV, related to C–C, C–O, C=O, and O=C–O, respectively [43, 44]. Figure 6c illustrates the high-resolution O 1s spectrum, which displayed three peaks for RGO-Ag@Co₃O₄ and Co₃O₄ and two peaks for RGO and RGO-Ag. Specifically, for Co₃O₄, the three peaks observed at 530 eV, 531.48 eV, and 532.58 eV were detailed to Co–O, C=O, and C–OH, respectively; for RGO-Ag@Co₃O₄, the 531.68 eV and 532.68 eV peaks corresponded to Co–O and C=O, respectively. A peak at 530.1 eV indicated the presence of Co–O–C, confirming the attachment of cobalt oxide to the RGO via strong covalent bonds [45].

The analysis investigated the O 1s band of RGO and RGO-Ag in the presence of Co₃O₄. This analysis revealed the presence of two peaks in the O 1s band at 531.28 eV

and 532.58 eV, which related to C=O and C–OH groups, respectively, similar to the RGO-Ag@Co₃O₄ [11]. The Co 2p spectrum, Fig. 6d, displayed two spin states, Co 2p_{3/2} and Co 2p_{1/2}, at 780.68 eV and 795.85 eV, respectively, with a 15.17 eV energy separation, which is indicative of mixed valence states. This enhanced electrochemical performance of the composite was recognized for this feature. Furthermore, the two main peaks of Co were deconvoluted into four separate peaks, 780.08 eV and 795.18 eV for Co³⁺ and 781.76 eV and 797.38 eV for Co²⁺. The presence of Co₃O₄ was confirmed by the four satellite peaks observed at 786.08 eV, 790.18 eV, 801.88 eV, and 805.98 eV [45, 46]. The Ag 3d spectrum, depicted in Fig. 6e, revealed two main peaks at 374.38 eV and 368.38 eV with 6 eV energy separation, indicative of metallic silver in the RGO-Ag@Co₃O₄. Other peaks observed in the two doublets, 3d 3/2 and 3d 5/2, were recognized to be silver oxides (AgO and Ag₂O). However, the metallic silver intensity was much higher than that of Ag⁺ and Ag⁺², indicating a small proportion of zero-valence silver conversion into oxides. The obtained results provide critical insights into the structural and compositional features of RGO-Ag@Co₃O₄, which could be used to optimize its electrochemical properties for various applications [11, 47, 48].

Electrochemical analysis

Cyclic voltammetry study

The electrochemical performance of the fabricated electrodes has been examined with a CV test. Using a two-electrode arrangement using 6M KOH as an aqueous electrolyte, the as-prepared composites (RGO, RGO-Ag, and RGO.Ag@Co₃O₄) were evaluated intensively. Figure 7 illustrates typical CV curves at different scan rates of 5–10 mV s^{−1} using a potential range of 0–1 V. The device’s storage capacity is expressed by the specific capacitance (Cs), which is represented through the following formulas [25, 26, 35, 49].

$$C = \int I(v)dv / \mu(v_f - v_i) \tag{1}$$

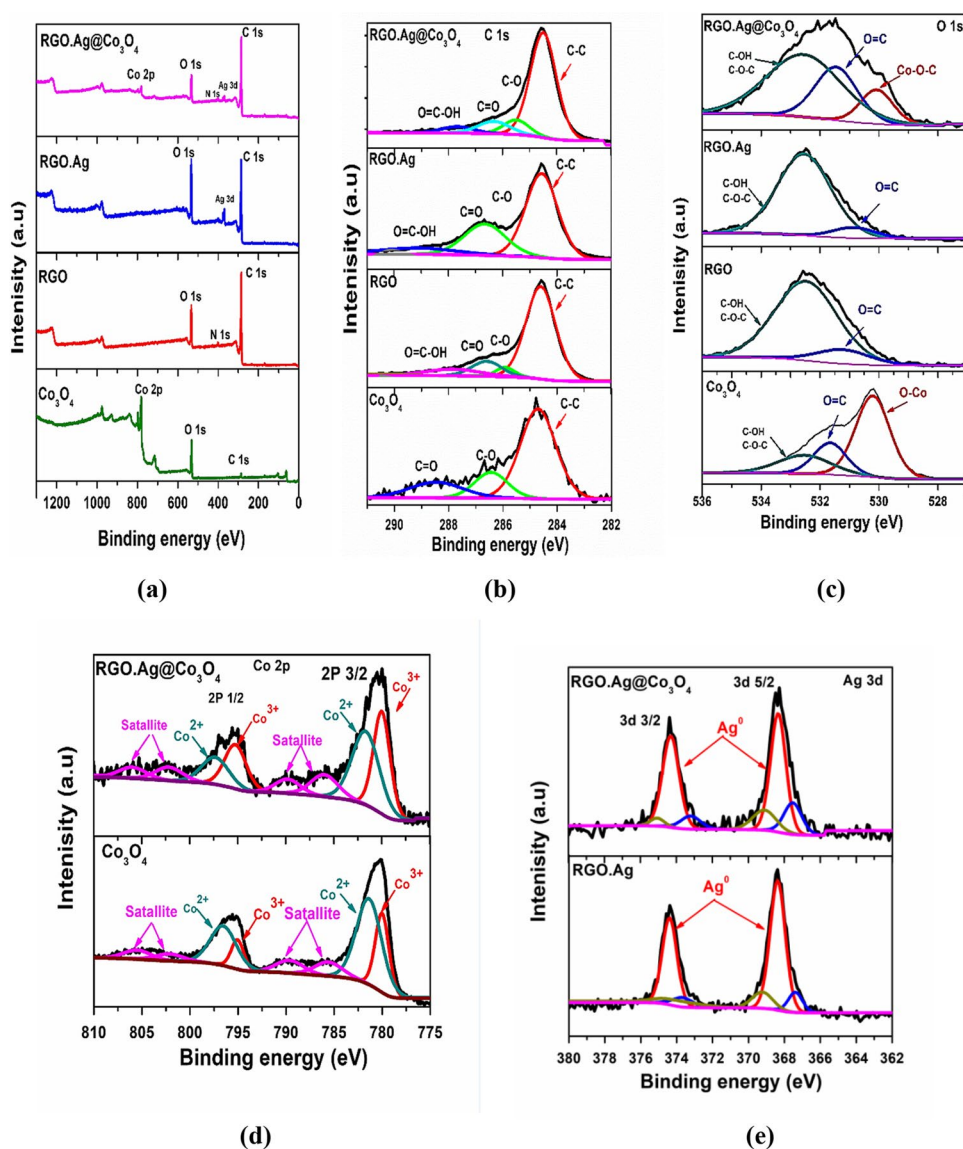
$$C_s = 4C/m \tag{2}$$

Here, $\int I(v) dv$ denotes the enclosed area of the curve, μ is the scan rate, $(v_f - v_i)$ denotes the potential range, and m denotes the effective mass in grams. In addition, the cyclic voltammetry (CV) chart for the Co₃O₄-based hybrid electrodes demonstrates a rectangular configuration, distinct from the anode and cathode peaks evident in the three-electrode test CV chart. Notably, the charging and discharging of these electrodes occur at a quasi-constant rate throughout

Table 1 Surface area characteristics of the synthesized materials

	S_{BET} (m ² /g)	Pore volume (cm ³ /g)	Mean pore diameter (nm)
RGO	8.4	6.97	33.2
RGO.Ag	9.01	5.3	23.68
RGO.Ag/Co ₃ O ₄	35.5	7.7	8.63

Fig. 6 XPS plots of **a** survey spectra, **b** C 1s, **c** O 1s, **d** Co 2p, and **e** Ag 3d for all synthesized materials



the voltammetric cycles, resulting in the absence of redox peaks in the recorded data [50–52].

The specific capacitances at a scan rate of 5 mV s^{-1} for RGO, RGO.Ag, and RGO.Ag@Co₃O₄ were found to be 142, 226.5, and 371.2 F g^{-1} , respectively. However, at a higher scan rate of 100 mV s^{-1} , the specific capacitances decreased to 104.7, 139.4, and 228.73 F g^{-1} , indicating an unprecedented capability rate. This decline suggests an inverse relationship between specific capacitance and scan rate, attributed to the reduced presence of electrolytic ions on the electrode contact as the scan rate increases, possibly due to the time required for electrode material diffusion. Comparisons of the Ag@Co₃O₄ curve with RGO and RGO.Ag in Fig. 7d reveal a larger percentage of the closed curve integral area at the same scan rate, implying higher energy storage. The nanostructure RGO.Ag@Co₃O₄ provides more electroactive sites related to the electrolyte, enhancing

capacitive performance. This superior performance emphasizes the homogenous distribution of Co₃O₄ in the RGO.Ag composite.

Moreover, Fig. 8 describes the GCD of the packed cell at C_d of 0.5, 1, 2, and 3 A g^{-1} and illustrates the value of the mass-specific capacitances of RGO, RGO.Ag, and RGO.Ag@Co₃O₄ are 114, 117.5, and 156 F g^{-1} , respectively, at 0.5 A g^{-1} . The nanocomposite electrode material exhibited a semi-triangle form, validating the electric double-layer performance. The results showed that the RGO.Ag@Co₃O₄ composite has the maximum discharge time. The C_s were found to be leading at low C_d because the surface of the electrode becomes more electroactive at low C_d .

In contrast, the diffusion is quick at high current density, reducing the C_s [25, 35]. The fabricated electrodes have a symmetrical triangle shape on all C_{ds} , demonstrating adequate columbic efficiency. The linearity of these curves was

Fig. 7 CV curves of **a** RGO, **b** RGO-Ag, and **c** RGO-Ag@Co₃O₄

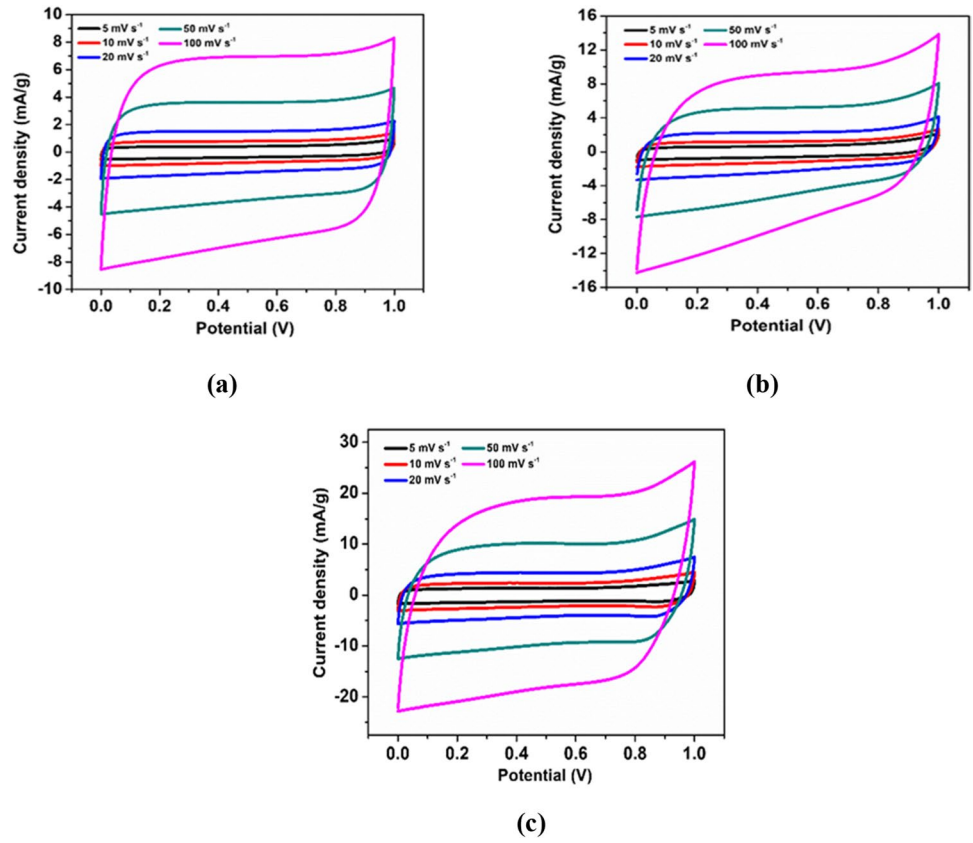
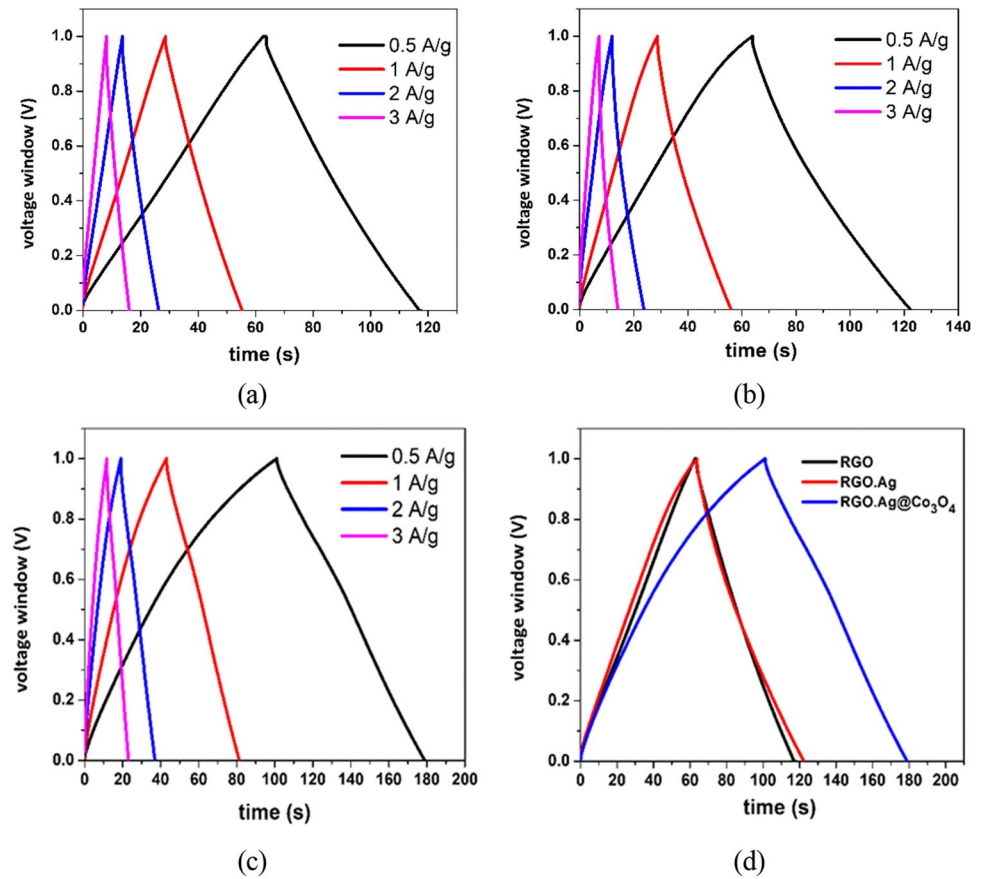


Fig. 8 GCD curves of **a** RGO, **b** RGO-Ag, **c** RGO-Ag@Co₃O₄, **d** comparative analysis of the different electrode materials at 0.5 A/g



used to evaluate the EDL mechanism. Because of the low internal resistance, the nanocomposite electrodes showed a minimal voltage drop. The optimum electrode material (RGO-Ag@Co₃O₄) demonstrated high reactivity and excellent energy storage performance.

Furthermore, galvanic charge–discharge (GCD) is a widely accepted method for calculating the capacitance, P_{ds}, and Eds of SCs, as it closely mimics the load behavior in most applications. Specific capacitance was calculated using the following formula [25, 35, 49]:

$$C_s = 4I * \Delta t / m \Delta V \quad (3)$$

where Δv represents the potential range, Δt represents the discharge time, I describes the current applied, and m represents the active material's total weight. Accordingly, GCD curves of the RGO and RGO-based composite electrodes at different C_{ds} are shown in Fig. 8. The RGO and RGO-Ag electrodes exhibited triangle-shaped curves, indicating typical electric double-layer performance. The electrodes exhibited no redox peaks, indicating EDL behavior's contribution [35, 49]. The specific capacitance values of all prepared active materials exist in Table 2. The highest specific capacitance value of 156 F g⁻¹ was obtained for RGO-Ag@Co₃O₄ at 0.5 A g⁻¹, consistent with the results obtained from CV investigations. On the other hand, at high current densities (3 A g⁻¹), the specific capacitance values decreased to 135 F g⁻¹ due to the limited ion diffusion rate. Furthermore, it is noteworthy that a slight decrease in voltage from 1 to ≥ 0.98 V was detected in all electrode materials employed in conjunction with the KOH electrolyte during the initial discharge process at 0.5 A g⁻¹. This voltage dew-drop is attributed to both the interior resistance and ESR of SCs and the obstruction of ion diffusion via a paper separator, resulting in the rising impedance [25].

In addition, EIS was examined on all materials in a frequency range of 0.1 Hz to 100 kHz to study the electrochemical performance of the electrode materials and the resistances accomplished with the electrode and electrolyte. The EIS results existed in the form of a Nyquist plot, which showed two distinct parts: a semi-circle in the high-frequency region and a straight line in the low-frequency region [53–55]. The EIS plots were utilized to fit the ESR to

determine the total impedance of the device, which consisted of the solution resistance (R_s) at the intercept with the x -axis, the charge transfer resistance (R_{ct}) at the end of the semi-circle, and the resistance in the pores (R_e) that was assessed by subtracting R_{ct} from R_s [35, 49]. Notably, the equivalent circuit attached to Fig. 9a shows a linear line observed in the low-frequency region of the Nyquist plot which is attributed to the ion diffusion within the electrode pores. This phenomenon can be effectively represented by the inclusion of Warburg resistance (W) in the equivalent circuit while R₁, R₂, and C₁ represent the Rs, Rct, and capacitance, respectively [56].

The electrode material values utilized in the SC were recorded and summarized in Table 3. The results revealed that adding silver NPs decreased the internal resistance and increased the cell capacitance of the SC. Besides, this study investigated the electrochemical cyclic behavior of various fabricated SCs and evaluated their suitability for practical applications [25, 26, 35]. Furthermore, doping with cobalt oxide diminished the internal resistance value, confirming increased specific capacitance, E_d, and P_d.

In addition, E_{ds} and P_{ds} were calculated via Eqs. 4 and 5 for all synthesized electrodes [25, 35]:

$$E_d(\text{Wh/kg}) = (C_s \times \Delta V^2) / 7.2 \quad (4)$$

$$P_d(\text{W/kg}) = (E_d / \Delta t) \times 3600 \quad (5)$$

where Δt is the discharged time, Fig. 9b demonstrates the Ragone plot of all RGO-based SCs in 6 M KOH [57, 58]. The as-prepared RGO-Ag@Co₃O₄ yielded the highest values, with an E_d of 21.6 Wh/kg and a P_d of 997 W/kg at 0.5 A g⁻¹. In addition, the lower electrochemical series resistances (ESRs) of RGO-Ag@Co₃O₄ directly contributed to the ideal electrode's higher E_d by enhancing the active regions of the electrode and increasing ion mobility [59, 60]. These results provide significant insights into the electrochemical performance of the synthesized electrodes and have substantial implications for enhancing high-performance SCs.

The capacitance retention of the fabricated devices was assessed through GCD cycling tests conducted at a substantial current density of 2 A g⁻¹, as illustrated in Fig. 9d. The RGO-Ag-based SCs demonstrated the highest retention, achieving a value of 91.59% after 2000 cycles. This high value of retention than RGO is given to the good distribution of silver nanoparticles into the graphene matrix, which heals the restacking nature of RGO and optimizes the capacitance retention. Interestingly, RGO-Ag@Co₃O₄ demonstrated stable retention over the initial 800 cycles and convenient capacitance retention of 85.79% after 2000 cycles. Moreover, it significantly provided the highest specific capacitance, making a promising electrode material for practical SC applications.

Table 2 The C_s data at different current densities

C _d (Ag ⁻¹)	Specific capacitance F/g		
	RGO	RGO-Ag	RGO-Ag@Co ₃ O ₄
0.5 Ag ⁻¹	108.6	117.5	156
1 Ag ⁻¹	104	108.24	152.5
2 Ag ⁻¹	96	94.4	143.6
3 Ag ⁻¹	87.2	84.6	135

Fig. 9 **a** EIS plots of RGO, RGO-Ag, and RGO-Ag@Co₃O₄, **b** Ragone plot of the packaged electrode materials, and **c** capacitance retention of the electrode materials

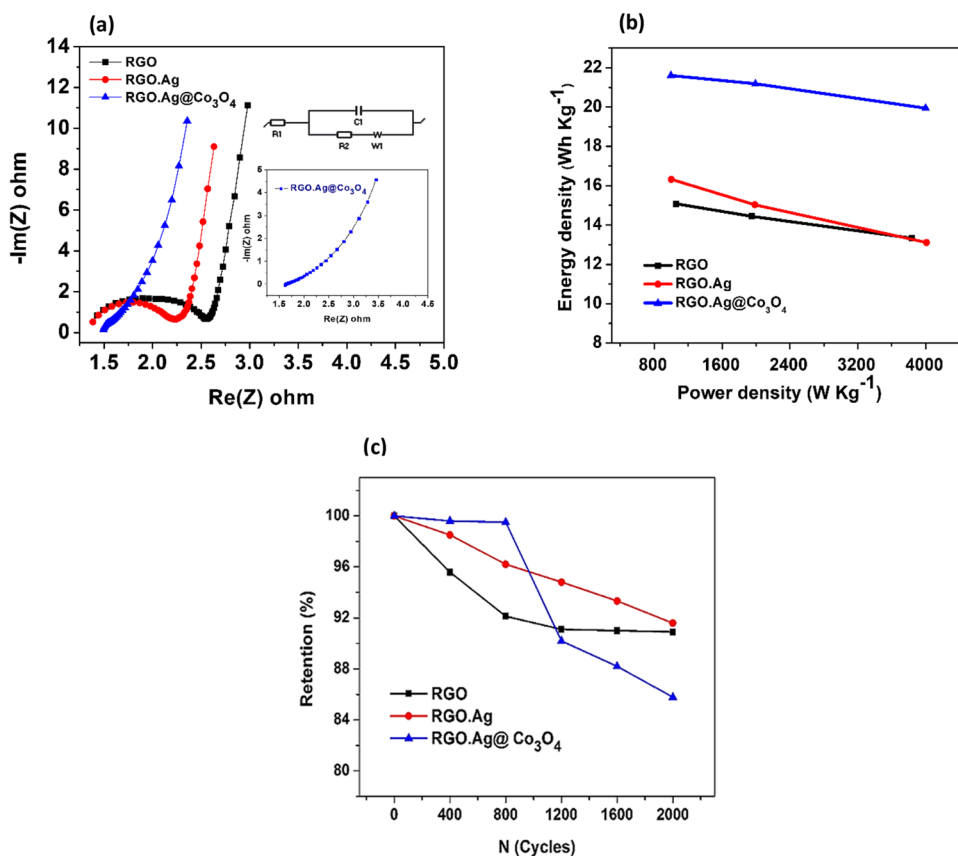


Table 3 The EIS of the fabricated cells

R (Ohm)	RGO	RGO-Ag	RGO-Ag@Co ₃ O ₄
R _s	1.37	1.26	1.53
R _{ct}	4.11	3.3	1.81
R _e	2.73	2.04	0.28

Conclusions

This study proved a new and efficient method for creating a high-performance SC based on a mechanochemical approach. This approach involves using a unique composite electrode of silver nanoparticles embedded in two-dimensional RGO and combined with cobalt oxide nanostructure. The dispersion of silver nanoparticles contributed to developing the graphene structure and improved the SC’s specific capacitance. The SEM and TEM micrographs show that the distribution of nanoparticles is homogenous between RGO layers, leading to enhanced surface area and improved storage capacity. In addition, The EDX results confirmed a successful preparation of RGO-Ag and RGO-Ag@Co₃O₄ materials. Furthermore, the electrode materials were conducted onto a Swagelok test cell with an aqueous electrolyte of 6 M KOH.

The specific capacitances of RGO, RGO-Ag, and RGO-Ag@Co₃O₄ were 142, 226.5, and 371.2 F g⁻¹, while the retentions were 90.5%, 91.59%, and 85.79%, respectively. It is worth mentioning that the prepared nanocomposite showed the lowest EIS, which enhanced the electrode’s active regions and increased ion mobility.

Supplementary Information The online version contains supplementary material available at <https://doi.org/10.1007/s11581-024-05385-9>.

Acknowledgements The authors acknowledge the Cairo University Faculty of Engineering, Metallurgical Engineering Laboratories, and Electronic Research Institute Nanotechnology Laboratory. Also, the authors acknowledge STDF funding support.

Author contribution “Conceptualization, Aliaa Abdelfattah, Fatma M. Ahmed, Lamiaa Z. Mohamed, Ahmed M. Selim; Methodology, Aliaa Abdelfattah, Fatma M. Ahmed, Lamiaa Z. Mohamed, Ahmed M. Selim; Software, NA; Validation, Aliaa Abdelfattah, Fatma M. Ahmed, Lamiaa Z. Mohamed, Ahmed M. Selim; Formal Analysis, Aliaa Abdelfattah, Fatma M. Ahmed, Lamiaa Z. Mohamed, Ahmed M. Selim; Investigation, Aliaa Abdelfattah, Fatma M. Ahmed, Lamiaa Z. Mohamed, Ahmed M. Selim; Resources, NA; Data Curation, Aliaa Abdelfattah, Fatma M. Ahmed, Lamiaa Z. Mohamed, Ahmed M. Selim; Writing-Original Draft Preparation, Aliaa Abdelfattah, Fatma M. Ahmed, Lamiaa Z. Mohamed, Ahmed M. Selim; Writing-Review & Editing, Aliaa Abdelfattah, Fatma M. Ahmed, Lamiaa Z. Mohamed, Ahmed M. Selim; Visualization, Aliaa Abdelfattah, Fatma M. Ahmed, Lamiaa Z. Mohamed, Ahmed M. Selim; Supervision, Aliaa Abdelfattah, Fatma M. Ahmed, Lamiaa Z. Mohamed, Ahmed M. Selim; Project Administration, Aliaa Abdelfattah, Fatma M. Ahmed, Lamiaa Z.

Mohamed, Ahmed M. Selim; Funding Acquisition, Aliaa Abdelfattah, Fatma M. Ahmed, Lamiaa Z. Mohamed, Ahmed M. Selim”.

Conceptualization: AA, FMA, LZM, and AMS; methodology: AA, FMA, LZM, and AMS; validation: AA, FMA, LZM, and AMS; formal analysis: AA, FMA, LZM, and AMS; investigation: AA, FMA, LZM, and AMS; data curation: AA, FMA, LZM, and AMS; writing—original, draft preparation: AA, FMA, LZM, and AMS; writing—review and editing: AA, FMA, LZM, and AMS; visualization: AA, FMA, LZM, and AMS; supervision: AA, FMA, LZM, and AMS; project administration: AA, FMA, LZM, and AMS; funding acquisition: AA, FMA, LZM, and AMS.

Funding Open access funding provided by The Science, Technology & Innovation Funding Authority (STDF) in cooperation with The Egyptian Knowledge Bank (EKB).

Data Availability The data supporting this study’s findings are available from the corresponding author upon reasonable request.

Declarations

Ethical approval This article does not contain any studies involving animals performed by any of the authors. Also, it does not include any studies of human participants performed by authors.

Competing interests The authors declare no competing interests.

Open Access This article is licensed under a Creative Commons Attribution 4.0 International License, which permits use, sharing, adaptation, distribution and reproduction in any medium or format, as long as you give appropriate credit to the original author(s) and the source, provide a link to the Creative Commons licence, and indicate if changes were made. The images or other third party material in this article are included in the article’s Creative Commons licence, unless indicated otherwise in a credit line to the material. If material is not included in the article’s Creative Commons licence and your intended use is not permitted by statutory regulation or exceeds the permitted use, you will need to obtain permission directly from the copyright holder. To view a copy of this licence, visit <http://creativecommons.org/licenses/by/4.0/>.

References

- Zhao J, Burke AF (2021) “Review on supercapacitors: technologies and performance evaluation”. *J Energy Chem* 59(July 1994):276–291. <https://doi.org/10.1016/j.jechem.2020.11.013>
- Barkholtz HM et al (2019) Multi-scale thermal stability study of commercial lithium-ion batteries as a function of cathode chemistry and state-of-charge. *J. Power Sources* 435(July):226777. <https://doi.org/10.1016/j.jpowsour.2019.226777>
- Kumar N, Bin Kim S, Lee SY, Park SJ (2022) “Recent advanced supercapacitor: a review of storage mechanisms, electrode materials, modification, and perspectives”. *Nanomaterials* 12(20). <https://doi.org/10.3390/nano12203708>
- Rasheed T (2022) MXenes as an emerging class of two-dimensional materials for advanced energy storage devices. *J Mater Chem A* 10(9):4558–4584. <https://doi.org/10.1039/d1ta10083a>
- Kumar R, Sahoo S, Joanni E, Singh RK (2022) A review on the current research on microwave processing techniques applied to graphene-based supercapacitor electrodes: an emerging approach beyond conventional heating. *J Energy Chem* 74:252–282. <https://doi.org/10.1016/j.jechem.2022.06.051>
- Smaism GF, Abed AM, Al-Madhhachi H, Hadrawi SK, Al-Khaateb HMM, Kianfar E (2023) Graphene-based important carbon structures and nanomaterials for energy storage applications as chemical capacitors and supercapacitor electrodes: a review, vol 13, no 1. Springer US
- Khandelwal M, Van Tran C, Lee J, Bin In J (2021) “Nitrogen and boron co-doped densified laser-induced graphene for supercapacitor applications”. *Chem Eng J* 428(May 2021):131119. <https://doi.org/10.1016/j.cej.2021.131119>
- Selim AM, Wasfey MA, Abdullallah HH, Zahran MB, Khalifa W, El-Mahallawi IS (2019) “Fabrication of supercapacitor based on reduced graphene oxide for energy storage applications”. *ACCS/PEIT 2019 - 2019 6th Int Conf Adv Control Circuits Syst 2019 5th Int Conf New Paradig Electron Inf Technol* 94–98. <https://doi.org/10.1109/ACCS-PEIT48329.2019.9062884>
- Dai Z, Ren P-G, Guo Z et al (2022) Silver nanoparticles as a conductive bridge for high-performance flexible all-solid-state asymmetric supercapacitor. *Int J Energy Res* 46(2):1813–1825. <https://doi.org/10.1002/er.7297>
- BabuPoudel M, Chandra Lohani P, Kim AA (2022) Synthesis of silver nanoparticles decorated tungsten oxide nanorods as high-performance supercapacitor electrode. *Chem Phys Lett* 804(January):139884. <https://doi.org/10.1016/j.cplett.2022.139884>
- Krishnaraj C et al (2022) Silver nanoparticles decorated reduced graphene oxide: eco-friendly synthesis, characterization, biological activities and embryo toxicity studies. *Environ Res* 210(December):112864. <https://doi.org/10.1016/j.envres.2022.112864>
- Ansari AR, Ansari SA, Parveen N, Ansari MO, Osman Z (2022) “Silver nanoparticle decorated on reduced graphene oxide-wrapped manganese oxide nanorods as electrode materials for high-performance electrochemical devices”. *Crystals* 12(3). <https://doi.org/10.3390/cryst12030389>
- Selim AM, Zahran MB, Khalifa W, El-Mahallawi IS (2021) “Facile synthesis of hybrid electrode materials based on RGO.Ag/Co for an efficient symmetric supercapacitor”. <https://doi.org/10.1016/j.jelechem.2021.115114>
- Gao D, Luo Z, Liu C, Fan S (2022) “A survey of hybrid energy devices based on supercapacitors”. *Green Energy Environ no. xxxx*. <https://doi.org/10.1016/j.gee.2022.02.002>
- Benoy SM, Pandey M, Bhattacharjya D, Saikia BK (2022) Recent trends in supercapacitor-battery hybrid energy storage devices based on carbon materials. *J Energy Storage* 52(PB):104938. <https://doi.org/10.1016/j.est.2022.104938>
- Zallouz S, Réty B, Vidal L, Le Meins JM, MateiGhimbeu C (2021) Co3O4 nanoparticles embedded in mesoporous carbon for supercapacitor applications. *ACS Appl Nano Mater* 4(5):5022–5037. <https://doi.org/10.1021/acsanm.1c00522>
- Umar A et al (2021) Perforated Co3O4 nanosheets as high-performing supercapacitor material. *Electrochim Acta* 389:138661. <https://doi.org/10.1016/j.electacta.2021.138661>
- Sharma S, Chand P (2023) “Supercapacitor and electrochemical techniques: a brief review”. *Results Chem* 5(November 2022):100885. <https://doi.org/10.1016/j.rechem.2023.100885>
- Dirican M, Yanilmaz M, Asiri AM, Zhang X (2020) “Polyaniline/MnO2/porous carbon nanofiber electrodes for supercapacitors”. *J Electroanal Chem* 861. <https://doi.org/10.1016/j.jelechem.2020.113995>
- Jun Hu, Yang P, Nie T, Liu S, Ni H, Shi J (2019) “Facile synthesis of NiO/nitrogen-doped reduced graphene oxide nanocomposites for the application in supercapacitors.” *Russ J Phys Chem A* 93(5):895–901. <https://doi.org/10.1134/S0036024419050145>
- Kong S et al (2019) MnO2 nanosheets decorated porous active carbon derived from wheat bran for high-performance asymmetric supercapacitor. *J Electroanal Chem* 850:113412. <https://doi.org/10.1016/j.jelechem.2019.113412>

22. Hun S (2011) Thermal reduction of graphene oxide. *Phys Appl Graphene - Exp*. <https://doi.org/10.5772/14156>
23. Abdolhosseinzadeh S, Asgharzadeh H, Kim HS (2015) Fast and fully-scalable synthesis of reduced graphene oxide. *Sci Rep* 5:1–7. <https://doi.org/10.1038/srep10160>
24. Li L et al (2013) Hydrothermal self-assembly synthesis of Mn₃O₄/reduced graphene oxide hydrogel and its high electrochemical performance for supercapacitors. *Chinese J Chem* 31(10):1290–1298. <https://doi.org/10.1002/cjoc.201300324>
25. Selim AM, Zahran MB, Khalifa W, El-Mahallawi IS (2021) Facile synthesis of hybrid electrode materials based on RGO.Ag/Co for an efficient symmetric supercapacitor. *J Electroanal Chem* 886(March):115114. <https://doi.org/10.1016/j.jelechem.2021.115114>
26. Elhamid AEMA, Alamin AA, Selim AM, Wasfey MA, Zahran MB (2019) “Fabrication of flexible, half printed and all-solid-state symmetric supercapacitor based on silver decorated reduced graphene oxide”. *ACCS/PEIT 2019 - 2019 6th Int Conf Adv Control Circuits Syst 2019 5th Int Conf New Paradig Electron Inf Technol* 151–155. <https://doi.org/10.1109/ACCS-PEIT48329.2019.9062877>
27. Stankovich S et al (2007) Synthesis of graphene-based nanosheets via chemical reduction of exfoliated graphite oxide. *Carbon N Y* 45(7):1558–1565. <https://doi.org/10.1016/j.carbon.2007.02.034>
28. Park S, An J, Potts JR, Velamakanni A, Murali S, Ruoff RS (2011) Hydrazine-reduction of graphite- and graphene oxide. *Carbon N Y* 49(9):3019–3023. <https://doi.org/10.1016/j.carbon.2011.02.071>
29. Prakash P, Gnanaprakasam P, Emmanuel R, Arokiyaraj S, Saravanan M (2013) Green synthesis of silver nanoparticles from leaf extract of *Mimusops elengi*, Linn. for enhanced antibacterial activity against multi drug resistant clinical isolates. *Colloids Surfaces B Biointerfaces* 108:255–259. <https://doi.org/10.1016/j.colsurfb.2013.03.017>
30. Wasfey MA et al (2020) Nickel cobaltite functionalized silver doped carbon xerogels as efficient electrode materials for high performance symmetric supercapacitor. *Materials (Basel)* 13(21):1–16. <https://doi.org/10.3390/ma13214906>
31. Tang XZ, Chen X, Wu G, Hu X, Yang J (2015) Improved chemical stability of silver by selective distribution of silver particles on reduced graphene oxide nanosheets. *RSC Adv* 5(61):49257–49262. <https://doi.org/10.1039/c5ra04508h>
32. Liu S et al (2020) A long life and high efficient rechargeable hybrid zinc-air/Co₃O₄ battery with stable high working voltage. *Ionics (Kiel)* 26(2):767–775. <https://doi.org/10.1007/s11581-019-03226-8>
33. Liu J, Jin R, Qiao Y, Wu Y, Wang X, Wang Y (2018) Determination of lead(II) using glassy carbon electrode modified with hexagonal Co₃O₄ microparticles. *Int J Electrochem Sci* 13(11):10415–10426. <https://doi.org/10.20964/2018.11.45>
34. Belles L, Moularas C, Smykała S, Deligiannakis Y (2021) “Flame spray pyrolysis co₃o₄/coo as highly-efficient nanocatalyst for oxygen reduction reaction”. *Nanomaterials* 11(4). <https://doi.org/10.3390/nano11040925>
35. Ahmed FM, Ateia EE, El-dek SI, El-kader SMA, Shafaay AS (2022) “Silver-substituted cobalt zeolite imidazole framework on reduced graphene oxide nanosheets as a novel electrode for supercapacitors”. *J Energy Storage* 55(PA):105443. <https://doi.org/10.1016/j.est.2022.105443>
36. Mohamedy MH, Sayed MM, Ahmed NM, Zahran MB (2020) High power capability of mos₂ based aqueous electrolyte supercapacitor. *Int J Nanoelectron Mater* 13(3):547–564
37. Ma X, Zare Y, Rhee KY (2017) “A two-step methodology to study the influence of aggregation/agglomeration of nanoparticles on young’s modulus of polymer nanocomposites”. *Nanoscale Res Lett* 12:0–6. <https://doi.org/10.1186/s11671-017-2386-0>
38. Ashraf MA, Peng W, Zare Y, Rhee KY (2018) “Effects of size and aggregation/agglomeration of nanoparticles on the interfacial/interphase properties and tensile strength of polymer nanocomposites”. *Nanoscale Res Lett* 13. <https://doi.org/10.1186/s11671-018-2624-0>
39. Liang X et al (2023) “α-Fe₂O₃-supported Co₃O₄ nanoparticles to construct highly active interfacial oxygen vacancies for ozone decomposition”. *Environ Pollut* 330(February):121704. <https://doi.org/10.1016/j.envpol.2023.121704>
40. Riaz R et al (2020) Activated charcoal and reduced graphene sheets composite structure for highly electro-catalytically active counter electrode material and water treatment. *Int J Hydrogen Energy* 45(13):7751–7763. <https://doi.org/10.1016/j.ijhydene.2019.06.138>
41. Yao T et al (2017) Effect of rGO coating on interconnected Co₃O₄ nanosheets and improved supercapacitive behavior of Co₃O₄/rGO/NF architecture. *Nano-Micro Lett* 9(4):1–8. <https://doi.org/10.1007/s40820-017-0141-9>
42. Sudhakar S, Joshi DN, Peera SG, Sahu AK, Eggleston CM, Prasath RA (2018) Hydrothermal-microwave synthesis of cobalt oxide incorporated nitrogen-doped graphene composite as an efficient catalyst for oxygen reduction reaction in alkaline medium. *J Mater Sci Mater Electron* 29(8):6750–6762. <https://doi.org/10.1007/s10854-018-8661-8>
43. Munde AV, Mulik BB, Dighole RP, Sathe BR (2020) Cobalt oxide nanoparticle-decorated reduced graphene oxide (Co₃O₄-rGO): active and sustainable nanoelectrodes for water oxidation reaction. *New J Chem* 44(36):15776–15784. <https://doi.org/10.1039/d0nj02598d>
44. Budak Ö, Uğuz Ö, Koca A (2021) Simultaneous electrochemical deposition of nickel cobalt oxide-reduced graphene oxide composites for high performance asymmetric supercapacitors. *J Energy Storage* 47(June):2022. <https://doi.org/10.1016/j.est.2021.103538>
45. Xu G et al (2022) A facile one-pot microwave assisted hydrothermal synthesis of hierarchical cobalt oxide/reduced graphene oxide composite electrode for high-performance supercapacitors. *J Alloys Compd* 897:163163. <https://doi.org/10.1016/j.jallcom.2021.163163>
46. Wang Q, Miao H, Sun S, Xue Y, Liu Z (2018) One-pot synthesis of Co₃O₄/Ag nanoparticles supported on n-doped graphene as efficient bifunctional oxygen catalysts for flexible rechargeable zinc–air batteries. *Chem - A Eur J* 24(55):14816–14823. <https://doi.org/10.1002/chem.201803236>
47. Jiao T et al (2015) Reduced graphene oxide-based silver nanoparticle-containing composite hydrogel as highly efficient dye catalysts for wastewater treatment. *Sci Rep* 5(March):1–12. <https://doi.org/10.1038/srep11873>
48. Sulaeman U, Suhendar S, Diastuti H, Andreas R, Yin S (2020) Short communication: Design of defect and metallic silver in silver phosphate photocatalyst using the hydroxyapatite and glucose. *Indones J Chem* 20(6):1441–1447. <https://doi.org/10.22146/ijc.48647>
49. Alamin AA, AbdElhamid AEM, Anis WR, Attiya AM (2019) Fabrication of symmetric supercapacitor based on relatively long lifetime polyaniline grown on reduced graphene oxide via Fe²⁺ oxidation sites. *Diam Relat Mater* 96:182–194. <https://doi.org/10.1016/j.DIAMOND.2019.05.013>
50. Zhang Y, Liu M, Sun S, Yang L (2020) The preparation and characterization of SnO₂/rGO nanocomposites electrode materials for supercapacitor. *Adv Compos Lett* 29(391):1–7. <https://doi.org/10.1177/2633366X20909839>
51. Liao Q, Li N, Jin S, Yang G, Wang C (2015) All-solid-state symmetric supercapacitor based on Co₃O₄ nanoparticles on vertically aligned graphene. *ACS Nano* 9(5):5310–5317. <https://doi.org/10.1021/acsnano.5b00821>

52. Yang L, Cheng S, Ding Y, Zhu X, Wang ZL, Liu M (2012) Hierarchical network architectures of carbon fiber paper supported cobalt oxide nanonet for high-capacity pseudocapacitors. *Nano Lett* 12(1):321–325. <https://doi.org/10.1021/nl203600x>
53. Wang Z et al (2020) Enhanced power density of a supercapacitor by introducing 3D-interfacial graphene. *New J Chem* 44(31):13377–13381. <https://doi.org/10.1039/d0nj02105a>
54. Lefterova E, Veleva S, Stoyanova A (2020) Impedance spectroscopy studies of the electrochemical hybrid supercapacitors based on activated carbon and iron oxides. *Bulg Chem Commun* 52:88–92
55. Mei BA, Munteshari O, Lau J, Dunn B, Pilon L (2018) Physical interpretations of Nyquist plots for EDLC electrodes and devices. *J Phys Chem C* 122(1):194–206. <https://doi.org/10.1021/acs.jpcc.7b10582>
56. Gaire M, Khatoon N, Chrisey D (2021) Preparation of cobalt oxide–reduced graphitic oxide supercapacitor electrode by photothermal processing. *Nanomaterials* 11(3):1–16. <https://doi.org/10.3390/nano11030717>
57. Numan A et al (2020) Facile sonochemical synthesis of 2D porous Co₃O₄ nanoflake for supercapattery. *J Alloys Compd* 819:153019. <https://doi.org/10.1016/j.jallcom.2019.153019>
58. Numan A et al (2022) Tailoring crystallinity of 2D cobalt phosphate to introduce pseudocapacitive behavior. *J Energy Storage* 54(5):105371. <https://doi.org/10.1016/j.est.2022.105371>
59. Iqbal J et al (2020) Cobalt oxide nanograins and silver nanoparticles decorated fibrous polyaniline nanocomposite as battery-type electrode for high performance supercapattery. *Polymers (Basel)* 12(12):1–19. <https://doi.org/10.3390/polym12122816>
60. Ahmed I et al (2022) “Evaluation of the synergistic effect of graphene oxide sheets and Co₃O₄ wrapped with vertically aligned arrays of poly(aniline-Co-melamine) nanofibers for energy storage applications”. *Polymers (Basel)* 14(13). <https://doi.org/10.3390/polym14132685>

Publisher's Note Springer Nature remains neutral with regard to jurisdictional claims in published maps and institutional affiliations.